Progress In Electromagnetics Research Letters, Vol. 103, 49–56, 2022

Compact Broadband 3 × 3 Nolen Matrix with Flat Output Ports Phase Differences

Hongmei Liu*, Hongxiao Zhang, Da Yu, Shaojun Fang, and Zhongbao Wang

Abstract—In the paper, a compact broadband 3×3 Nolen matrix with flat output ports phase differences is presented. By using two types of three-branch quadrature couplers, wideband impedance matching and flat output ports amplitudes are obtained. Besides, imbalanced output ports phase differences are compensated by inserting two differential phase shifters between the couplers. Design equations for the proposed structure are derived, and influences of the two differential phase shifters on the phase differences of the Nolen matrix are investigated. To verify the effectiveness of the structure, a prototype operating at 5.8 GHz is fabricated and measured. Measurement results agree well with the simulated ones. Fractional bandwidths (FBWs) of 31.21% and 45.17% are obtained for 15-dB return loss and 15-dB isolation. Moreover, under the criterions of amplitude imbalance < 1 dB and phase difference $< 5°$, the measured FBWs are more than 23.20% and 23.96%, respectively.

1. INTRODUCTION

Beamforming networks (BFNs), which extend the operations of single beam from the antenna array to multiple fixed beams, are of interest for applications including fifth-generation (5G) communications, collision avoidance systems, and internet of things (IoT). Butler [1–3], Blass [4, 5], and Nolen [6, 7] matrices are the most popular solutions for circuit-based BFNs. In the standard form, the Butler matrix generates 2^N beams, while the Blass and Nolen matrices can provide arbitrary number of beams, which are more flexible. The Blass matrix is less attractive due to the low power efficiency caused by the loads at the terminations. As a modification, the Nolen matrix is presented to suppress the termination loads in the Blass matrix, which is theoretically lossless. Besides, more than half of the components from the Blass matrix is cut. In a word, the Nolen matrix simplifies the structure of Blass matrix and reduces the loss of energy. Compared with the Butler matrix, same functions can be obtained by the Nolen matrix without using the crossovers. Nolen matrix can realize an arbitrary number of ports. Thus, the Nolen matrix has great study space and practical applications.

Although the Nolen matrix has great advantages, few researches have been explored. In [7], a 4×4 Nolen matrix with the same excitations of a Butler matrix is designed at S-band. The fundamental theory of Nolen matrix is introduced with narrow bandwidth. Later, SIW technique [8, 9] is applied in realization to improve the bandwidth. In [8], the performances are investigated over a 500-MHz frequency bandwidth ranging from 12.25 to 12.75 GHz. The design in [9] achieves results over a 11.7% frequency bandwidth centered at 77 GHz. Recently, novel uniplanar Nolen matrices with asymmetrical [10, 11] and symmetrical [12] output ports phase differences are reported. For example, by using quadrature couplers with special couplings and phase delay lines, a miniaturized 3×3 Nolen matrix with phase differences of $-90°$, $150°$, and $30°$ is designed [11]. A fractional bandwidth (FBW) of 8% is obtained under the criterion of more than 10-dB return loss (RL) and $\pm 4.1°$ phase imbalance. Later, by using 180° couplers, symmetrical phase differences ($-120°$, $0°$, and $120°$) with 9.55% FBW

Received 22 November 2021, Accepted 15 February 2022, Scheduled 22 February 2022

* Corresponding author: Hongmei Liu (lhm323@dlmu.edu.cn).
The authors are with the Dalian Maritime University, Dalian 116026, Liaoning, China.

(RL > 10 dB) can be obtained in [12]. However, the bandwidths for ±10° phase tolerance are narrow (5.03% for port 1, 1.56% for port 2, and 1.56% for port 3). Due to the influence of the phase delay lines, the recently reported Nolen matrices [10–12] also exhibit a narrow bandwidth. To compensate for the worse phase variations of [12], two 90° phase shifters are added in [13]. After the compensation, the ±10° phase tolerance bandwidths are increased to 10.86%, 12.41% and 24.48 % for ports 1, 2, and 3 excitations, respectively. In summary, the designed Nolen matrices [7–13] are operated in narrow frequency range (around 10%), which limits the applications in high-rate communication. Specifically, the bandwidth for phase responses is more important to avoid the beam squint problem in wideband systems.

In the letter, a broadband 3×3 Nolen matrix with flat output ports phase differences (PDs) is presented. Wideband operation is realized by using three-branch couplers with the couplings of 1.76 dB and 3 dB. To compensate for the wideband phase variations, two differential phase shifters (D-PSs) are inserted. In Section 2, closed-form equations are derived for the wideband operation. In Section 3, a prototype with PDs of $-90°$, 150°, and 30° is designed, fabricated, and measured. The measured results show that obvious bandwidth enhancements in the items of 15-dB RL, 1-dB amplitude (AP) imbalance, and 5° PD are realized by the proposed structure. Finally, the paper is concluded in Section 4.

2. THEORETICAL ANALYSIS

The schematic of the proposed 3×3 Nolen matrix is shown in Fig. 1, which includes three input ports (P1–P3) and three output ports (P4P6). The proposed 3×3 Nolen matrix is composed of two three-branch couplers named as BL-C1 and BL-C2, and two D-PSs named as D-PS1 and D-PS2. The coupling coefficients of the two couplers are $k1$ and $k2$, respectively. The two D-PSs share the same reference line with the electrical length of θ_1. The main line of D-PS1 with the phase of θ_2 is connected between two BL-C2 couplers, while the main line of D-PS2 with the phase of θ_3 is connected between the BL-C1 coupler and port P4. In the design, the main lines of the two D-PSs are composed by open/short-circuit loaded transmission lines. In the main line of D-PS1, the phase of θ_2 is formed by one transmission line (θ_{11}, Z_{11}), two open-circuited lines (θ_{12}, Z_{12}), and two short-circuited lines (θ_{13}, Z_{13}). Similarly, the phase of θ_3 in the main line of D-PS2 is formed by one transmission line (θ_{21}, Z_{21}), two open-circuited lines (θ_{22}, Z_{22}), and two short-circuited lines (θ_{23}, Z_{23}). The system characteristic impedance is defined as Z_0.

Firstly, according to the structures in the main lines of D-PS1 and D-PS2, the S-parameters ($S_{7,7}$,

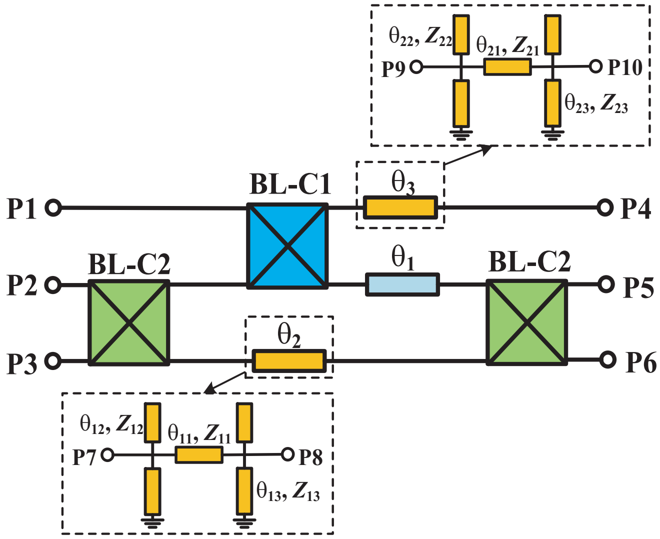

Figure 1. The schematic diagram of the proposed 3×3 Nolen matrix.

$S_{8,7}$, $S_{9,9}$, and $S_{10,9}$) for the two lines can be derived, as shown in Eq. (1).

$$S_{7,7} = \frac{\mathrm{j}\left(\frac{\sin\theta_{11}Z_{11}}{Z_0} - 2a_1\cos\theta_{11}Z_0 - \frac{\sin\theta_{11}Z_0}{Z_{11}} + a_1^2\sin\theta_{11}Z_{11}Z_0\right)}{\left[2\left(\cos\theta_{11} - a_1\sin\theta_{11}Z_{11}\right) + \mathrm{j}\left(\frac{\sin\theta_{11}Z_{11}}{Z_0} + 2a_1\cos\theta_{11}Z_0 + \frac{\sin\theta_{11}Z_0}{Z_{11}} - a_1^2\sin\theta_{11}Z_{11}Z_0\right)\right]} \tag{1a}$$

$$S_{8,7} = \frac{2}{\left[2\left(\cos\theta_{11} - a_1\sin\theta_{11}Z_{11}\right) + \mathrm{j}\left(\frac{\sin\theta_{11}Z_{11}}{Z_0} + 2a_1\cos\theta_{11}Z_0 + \frac{\sin\theta_{11}Z_0}{Z_{11}} - a_1^2\sin\theta_{11}Z_{11}Z_0\right)\right]} \tag{1b}$$

$$S_{9,9} = \frac{\mathrm{j}\left(\frac{\sin\theta_{21}Z_{11}}{Z_0} - 2a_2\cos\theta_{21}Z_0 - \frac{\sin\theta_{21}Z_0}{Z_{21}} + a_2^2\sin\theta_{21}Z_{21}Z_0\right)}{\left[2\left(\cos\theta_{21} - a_2\sin\theta_{21}Z_{21}\right) + \mathrm{j}\left(\frac{\sin\theta_{21}Z_{21}}{Z_0} + 2a_2\cos\theta_{21}Z_0 + \frac{\sin\theta_{21}Z_0}{Z_{21}} - a_2^2\sin\theta_{21}Z_{21}Z_0\right)\right]} \tag{1c}$$

$$S_{10,9} = \frac{2}{\left[2\left(\cos\theta_{21} - a_2\sin\theta_{21}Z_{21}\right) + \mathrm{j}\left(\frac{\sin\theta_{21}Z_{21}}{Z_0} + 2a_2\cos\theta_{21}Z_0 + \frac{\sin\theta_{21}Z_0}{Z_{21}} - a_2^2\sin\theta_{21}Z_{21}Z_0\right)\right]} \tag{1d}$$

where

$$a_1 = \frac{\tan\theta_{12}}{Z_{12}} - \frac{\cot\theta_{13}}{Z_{13}} \tag{2a}$$

$$a_2 = \frac{\tan\theta_{22}}{Z_{22}} - \frac{\cot\theta_{23}}{Z_{23}} \tag{2b}$$

Then, the phases of θ_2 and θ_3 can be obtained as

$$\theta_2 = \angle S_{8,7} = -\arctan\frac{\left[\frac{\sin\theta_{11}Z_{11}}{Z_0} + 2a_1\cos\theta_{11}Z_0 + \frac{\sin\theta_{11}Z_0}{Z_{11}} - a_1^2\sin\theta_{11}Z_{11}Z_0\right]}{2(\cos\theta_{11} - a_1\sin\theta_{11}Z_{11})} \tag{3a}$$

$$\theta_3 = \angle S_{10,9} = -\arctan\frac{\left[\frac{\sin\theta_{21}Z_{21}}{Z_0} + 2a_2\cos\theta_{21}Z_0 + \frac{\sin\theta_{21}Z_0}{Z_{21}} - a_2^2\sin\theta_{21}Z_{21}Z_0\right]}{2\left(\cos\theta_{21} - a_2\sin\theta_{21}Z_{21}\right)} \tag{3b}$$

Secondly, the relations of the parameters in the 3 × 3 Nolen matrix are analyzed. For example, when port 1 is excited, the output amplitudes of ports P4, P5, and P6 can be expressed as $1 - k1$, $k1 \times (1 - k2)$, and $k1 \times k2$, respectively. To obtain equal output amplitude, the values of $k1$ and $k2$ are calculated as 2/3 and 1/2, separately, corresponding to the couplings of 1.76 dB and 3 dB.

Equations (4)–(6) show the S-parameters of the 3 × 3 Nolen matrix when different input ports are excited.

$$S_{41} = e^{j[\pi-\theta_3]} \tag{4a}$$

$$S_{51} = e^{j\left[-\frac{2}{\pi}-\theta_1\right]} \tag{4b}$$

$$S_{61} = e^{j[\pi-\theta_1]} \tag{4c}$$

$$S_{42} = e^{j\left[-\frac{2}{\pi}-\theta_3\right]} \tag{5a}$$

$$S_{52} = -\frac{1}{2}e^{-j\theta_1} - \frac{\sqrt{3}}{2}e^{-j\theta_2} \tag{5b}$$

$$S_{62} = \frac{1}{2}e^{j\left[\frac{\pi}{2}-\theta_1\right]} - \frac{\sqrt{3}}{2}e^{j\left[\frac{\pi}{2}-\theta_2\right]} \tag{5c}$$

$$S_{43} = e^{j[\pi-\theta_3]} \tag{6a}$$

$$S_{53} = \frac{1}{2}\mathrm{e}^{\mathrm{j}\left[\frac{\pi}{2}-\theta_1\right]} + \frac{\sqrt{3}}{2}\mathrm{e}^{\mathrm{j}\left[-\frac{\pi}{2}-\theta_2\right]} \tag{6b}$$

$$S_{63} = \frac{1}{2}\mathrm{e}^{-\mathrm{j}\theta_1} + \frac{\sqrt{3}}{2}\mathrm{e}^{-\mathrm{j}\theta_2} \tag{6c}$$

The output ports phase differences $\Delta\phi_1$, $\Delta\phi_2$, and $\Delta\phi_3$ for ports P1, P2, and P3 excitations can be obtained.

$$\Delta\phi_1 = \angle S_{51} - \angle S_{41} = \angle S_{61} - \angle S_{51} \tag{7a}$$

$$\Delta\phi_2 = \angle S_{52} - \angle S_{42} = \angle S_{62} - \angle S_{52} \tag{7b}$$

$$\Delta\phi_3 = \angle S_{53} - \angle S_{43} = \angle S_{63} - \angle S_{53} \tag{7c}$$

Substituting Eqs. (4)–(6) into Eq. (7), the relationships among θ_1, θ_2, and θ_3 are derived

$$\theta_2 - \theta_1 = \pm\frac{\pi}{2} \tag{8a}$$

$$\theta_3 - \theta_1 = \pi \tag{8b}$$

Then, substituting Eq. (8) into Eq. (3) under the condition of $S_{7,7} = S_{9,9} = 0$ for ideal matching, the parameters relationships of the two D-PSs can be expressed, as listed in Eq. (9).

$$\frac{\tan\theta_{12}}{Z_{12}} - \frac{\cot\theta_{13}}{Z_{13}} = \frac{1}{\tan\theta_{11}Z_{11}} - \frac{1}{Z_0\tan\left(\theta_1 \pm \frac{\pi}{2}\right)} \tag{9a}$$

$$\frac{\tan\theta_{22}}{Z_{22}} - \frac{\cot\theta_{23}}{Z_{23}} = \frac{1}{\tan\theta_{21}Z_{21}} - \frac{1}{Z_0\tan\left(\theta_1 + \pi\right)} \tag{9b}$$

According to Eq. (9), the phase variations of the Nolen matrix can be compensated by selecting suitable parameter values of the two D-PSs. Since six unknowns exist in the main lines of both D-PS1 and D-PS2, some of the unknowns are preassigned for easy calculation. In the following, an example is designed, and detailed procedures are provided.

3. IMPLEMENTATION AND MEASUREMENT

In this section, a prototype is designed at 5.8 GHz for validation. Here, the value of θ_1 is set as 180°, then θ_2 and θ_3 are calculated as 90° and 360°, respectively. In the design, for the structure forming a phase shift of θ_2, the characteristic impedances of the transmission lines are all equal to Z ($Z_{11} = Z_{12} = Z_{13} = Z = 50\,\Omega$), and the value of θ_{11} is equal to θ_2. Substituting the assigned values into Eq. (9a), the relationship between θ_{12} and θ_{13} can be derived as Eq. (10a). Similarly, for the structure forming a phase shift of θ_3, the following parameters are preassigned: $Z_{21} = Z_0$, $\theta_{22} = \theta_{23} = \lambda/4$, $\theta_{21} = \theta_3$. Substituting the assigned values into Eq. (9b), the relationship between Z_{22} and Z_{23} can be derived as (10b).

$$\tan\theta_{12} - \cot\theta_{13} = 0 \tag{10a}$$

$$Z_{22} = Z_{23} \tag{10b}$$

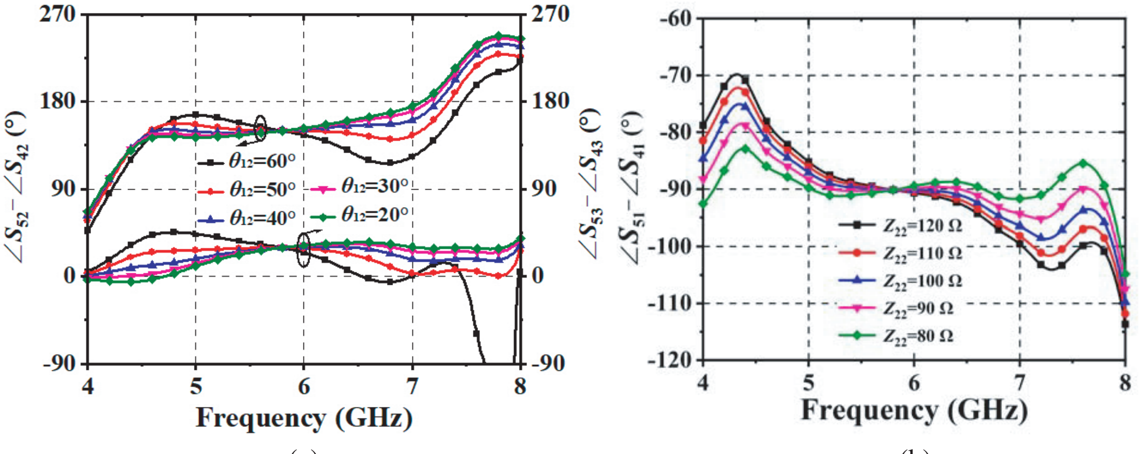

(a) (b)

Figure 2. Output ports phase difference for different values of (a) θ_{12} and (b) Z_{22}.

It is noted that the parameters in D-PS1 mainly influence the phase flatness between output ports P4 and P5 when P2 or P3 is excited. Then, the PDs between ports P4 and P5 under ports P2 and P3 excitation are plotted for different values of θ_{12}, as shown in Fig. 2(a). It is observed that when the value of θ_{12} increases from 30° to 70° with 10° interval, the FBWs for PD $= 30° \pm 5°$ are 27.24%, 23.28%, 29.48%, 9%, and 2.41%, respectively, under P2 excitation. And the values are 27.41%, 32.34%, 25.86%, 8.28%, and 2.24% when P3 is excited (PD $= 150° \pm 5°$). Consider more flat phase difference under both P2 and P3 excitations, the value of θ_{12} is chosen as 30°. According to Eq. (10a), θ_{13} is calculated as 60°.

Since the parameters in D-PS2 mainly influence the phase flatness between output ports P5 and P4 when P1 excited, the PDs between ports P5 and P4 ($\angle S_{51} - \angle S_{41}$) with different values of Z_{22} are given in Fig. 2(b). It is observed that when the value of Z_{22} increases from 80 Ω to 120 Ω with 10 Ω interval, the FBWs for PD $= -90° \pm 5°$ are 39.14%, 35.86%, 33.45%, 31.21%, and 29.31%, respectively. Thus, the value of Z_{22} is chosen as 80 Ω for wider PD FBW.

Based on the calculated values, the prototype is designed and optimized on an F4B substrate ($\varepsilon_r = 3.5$, $\tan\delta = 0.0035$, $h = 0.8\,\text{mm}$). Fig. 3 shows a photograph of the designed prototype with an overall size of 75 mm × 50 mm. Figs. 4–6 show the simulated and measured results, which agree with each other. As shown in Fig. 4, the measured FBWs of 31.21% and 45.17% are obtained for 15-dB RL and isolation (IO), respectively. In the simulation, the FBWs are 32.59% and 43.28%. For port P1 excitation, the measured FBWs for AP < 1 dB and PD $= -90° \pm 5°$ are 26.56% (5.06 ∼ 6.61 GHz) and 29.91% (5.23 ∼ 7.07 GHz), respectively. When port P2 is excited, the measured FBWs are 25.46% (5.14 ∼ 6.64 GHz) and 26.27% (5.29 ∼ 6.89 GHz) under the criterions of AP < 1 dB and PD $= 150° \pm 5°$, respectively, while the FBWs for port 3 excitation are 23.20% (5.03 ∼ 6.35 GHz) and 23.96% (5.29 ∼ 6.73 GHz) with AP < 1 dB and PD $= 30° \pm 5°$, respectively. Table 1 shows the detailed bandwidths including the simulated results.

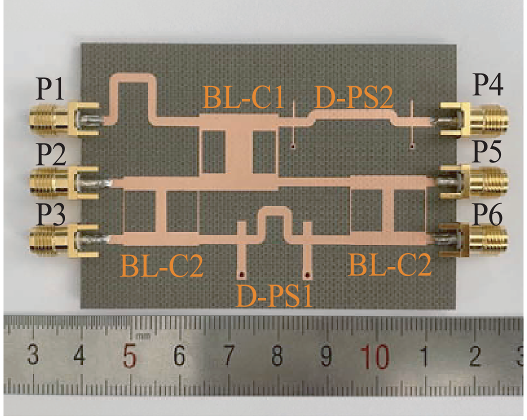

Figure 3. Photograph of the designed 3 × 3 Nolen matrix.

Table 1. Simulated and measured FBW results.

Excitation	Results	FBW (%)	
		AP < 1 dB	PD $< 5°$
P1	Simu.	26.03	34.31
	Meas.	26.56	29.91
P2	Simu.	28.97	26.03
	Meas.	25.46	26.27
P3	Simu.	26.21	26.03
	Meas.	23.20	23.96

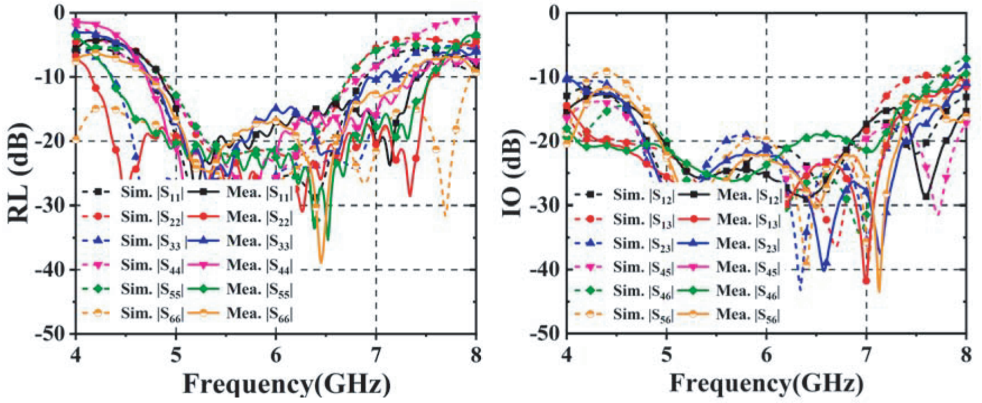

(a) (b)

Figure 4. Simulated and measured (a) RLs and (b) IOs.

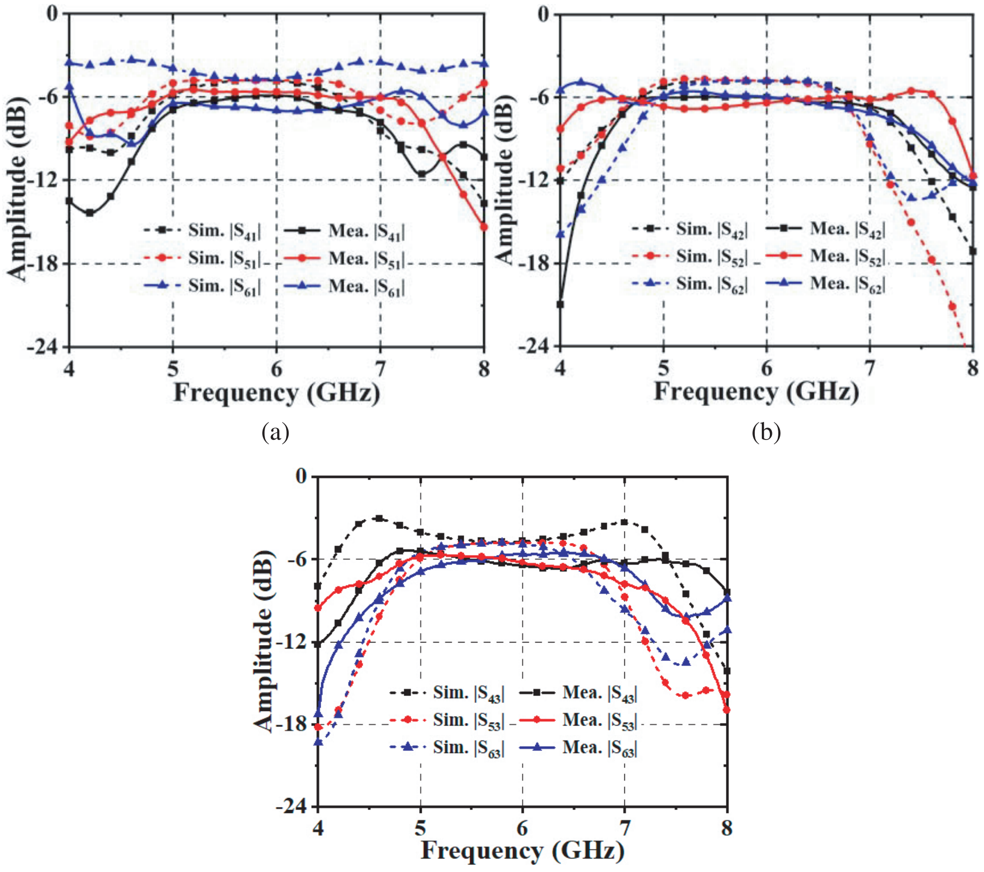

(a) (b)

(c)

Figure 5. Simulated and measured output ports amplitudes under different excitations. (a) Port P1. (b) Port P2. (c) Port P3.

Table 2 compares the performances of the proposed Nolen matrix with several representative reports. Obvious bandwidth enhancements in the items of 15-dB RL, 1-dB AP, and 5° PD are realized by the proposed structure compare with other Nolen matrices, which indicates a good candidate in applications of BFNs for wideband multi-beam antennas.

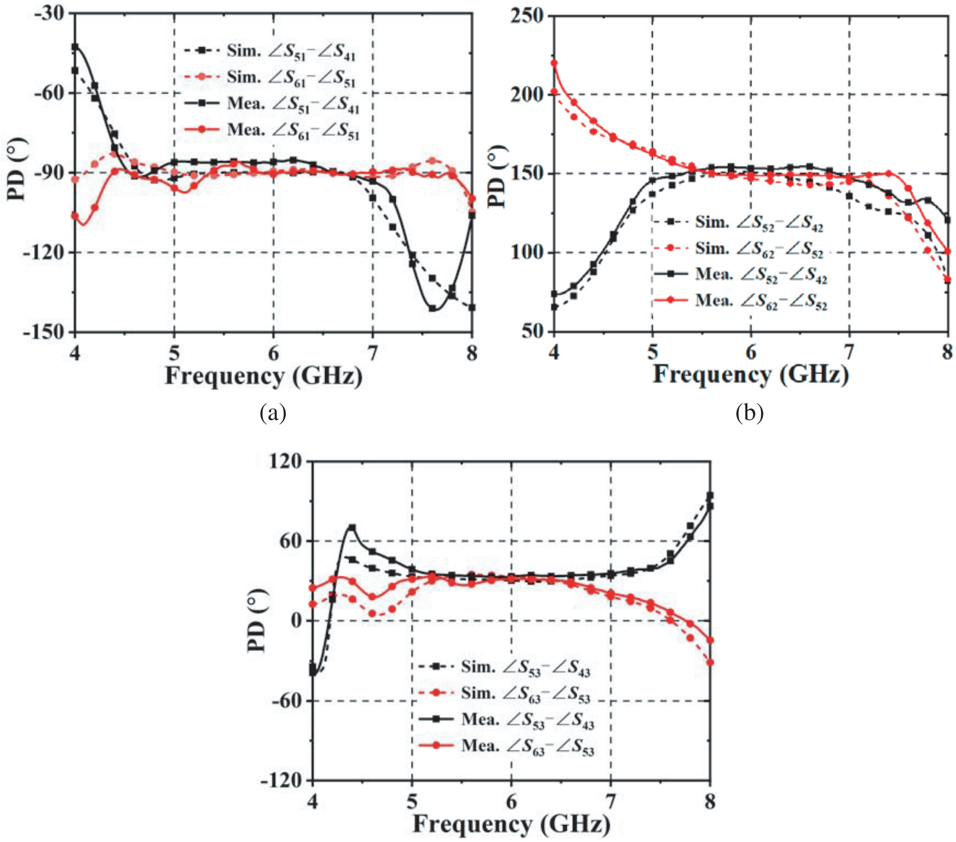

(a) (b)

(c)

Figure 6. Simulated and measured output ports PDs under different excitations. (a) Port P1. (b) Port P2. (c) Port P3.

Table 2. Performance comparisons among the proposed and representative Nolen matrix.

Ref.	Freq. (GHz)	FBW (%)			Size ($\lambda_g \times \lambda_g$)
		RL > 15 dB	AP < 1 dB	PD < 5°	
[7]	2.2	–	3.97	1.44	–
[8]	12.5	8.33	12.07	7.59	8.73×6.69
[10]	1	6.51	3.9^a	6.89	0.29×0.10
[11]	5.8	2.24	3.33	2.43	2.37×1.05
[12]	5.8	0.5	3.99	1.56	3.16×2.76
[13]	5.8	–	–	10.86^b	–
This work	**5.8**	**31.21**	**23.20**	**23.96**	$\mathbf{2.72 \times 2.0}$

^{a} AP < 2 dB. ^{b} PD < 10°.

4. CONCLUSION

In this paper, a broadband 3×3 Nolen matrix with flat output ports phase differences is presented, which is composed of wideband quadrature couplers with two types of differential phase shifters. Thanks to the differential phase shifters, the phase slopes of different output ports are compensated, resulting in flat output ports phase differences. Measurement results indicate that the proposed structure can be a good candidate for wideband multi-beam antennas BFNs.

ACKNOWLEDGMENT

This work was supported in part by the National Natural Science Foundation of China under Grant 51809030, in part by the Natural Science Foundation of Liaoning Province under Grant 2020-MS-127, in part by the Liaoning Revitalization Talents Program under Grant XLYC2007067, in part by the Dalian Youth Science and Technology Star Project under Grant 2020RQ007 and in part by the Fundamental Research Funds for the Central Universities under Grant 3132021231.

REFERENCES

1. Tajik, A. S., and M. Fakharzadeh, "Asymmetrical 4 × 4 Butler matrix and its Application for single layer 8×8 Butler matrix," *IEEE Transactions on Antennas and Propagation*, Vol. 67, No. 8, 5372–5379, Aug. 2019.
2. Liu, H., S. Fang, Z. Wang, and S. Fu, "Design of arbitrary-phase-difference transdirectional coupler and its application to a flexible Butler matrix," *IEEE Transactions on Microwave Theory and Techniques*, Vol. 67, No. 10, 4175–4185, Oct. 2019.
3. Xiang, K., F. Chen, Q. Chu, and M. J. Lancaster, "A broadband 3 × 4 Butler matrix and its application in multibeam antenna arrays," *IEEE Transactions on Antennas and Propagation*, Vol. 67, No. 12, 7622–7627, Dec. 2019.
4. Chen, P., W. Hong, Z. Kuai, and J. Xu, "A double layer substrate integrated waveguide Blass matrix for beamforming applications," *IEEE Microwave and Wireless Components Letters*, Vol. 19, No. 6, 374–376, Jun. 2009.
5. Tsokos, et al., "Analysis of a multibeam optical beamforming network based on Blass matrix architecture," *Journal of Lightwave Technology*, Vol. 36, No. 16, 3354–3372, Aug. 15, 2018.
6. Fonseca, N. J. G., "Study and design of a s-band 4 × 4 Nolen matrix for satellite digital multimedia broadcasting applications," *2006 12th International Symposium on Antenna Technology and Applied Electromagnetics and Canadian Radio Sciences Conference*, 1–4, 2006.
7. Fonseca, N. J. G., "Printed S-band 4 × 4 Nolen matrix for multiple beam antenna applications," *IEEE Transactions on Antennas and Propagation*, Vol. 57, No. 6, 1673–1678, Jun. 2009.
8. Djerafi, T., N. J. G. Fonseca, and K. Wu, "Planar Ku-band 4×4 Nolen matrix in SIW technology," *IEEE Transactions on Microwave Theory and Techniques*, Vol. 58, No. 2, 259–266, Feb. 2010.
9. Djerafi, T., N. J. G. Fonseca, and K. Wu, "Broadband substrate integrated waveguide 4 × 4 Nolen matrix based on coupler delay compensation," *IEEE Transactions on Microwave Theory and Techniques*, Vol. 59, No. 7, 1740–1745, Jul. 2011.
10. Ren, H., H. Zhang, and B. Arigong, "Ultra-compact 3 × 3 Nolen matrix beamforming network," *IET Microw. Antennas Propag.*, Vol. 14, No. 3, 143–148, Jan. 2020.
11. Ren, H., H. Zhang, Y. Jin, Y. Gu, and B. Arigong, "A novel 2-D 3 × 3 Nolen matrix for 2-D beamforming applications," *IEEE Transactions on Microwave Theory and Techniques*, Vol. 67, No. 11, 4622–4631, Nov. 2019.
12. Li, P., H. Ren, and B. Arigong, "A symmetric beam-phased array fed by a Nolen matrix using 180° couplers," *IEEE Microwave and Wireless Components Letters*, Vol. 30, No. 4, 387–390, Apr. 2020.
13. Li, P., H. Ren, and B. Arigong, "A uniplanar 3 × 3 Nolen matrix beamformer with beam squint reduction," *2020 IEEE International Symposium on Antennas and Propagation and North American Radio Science Meeting*, 515–516, 2020.